Journal of Alloys and Compounds 1036 (2025) 182072

Contents lists available at ScienceDirect

Journal of Alloys and Compounds

journal homepage: www.elsevier.com/locate/jalcom

Tailoring heterogeneous grain and phase distributions to enhance mechanical properties of TRIP-type $Fe_{50}Mn_{30}Co_{10}Cr_{10}$ high-entropy alloys through flash Joule annealing

Changshan Zhou [a,b,c], Qingwei Gao [b,c,*], Jianhong Gong [b,c], Pingping Liu [b,c], Jiyao Zhang [b,c], Xiqiang Wang [a,c], Zhijie Yan [a,d,**], Xiaoliang Han [b,c], Kaikai Song [a,b,c,**]

[a] School of Materials Science and Engineering, North University of China, Taiyuan 030051, China
[b] School of Mechanical, Electrical & Information Engineering, Shandong University, Weihai 264209, China
[c] Weihai Research Institute of Industrial Technology, Shandong University, Weihai 264209, China
[d] Shanxi Key Laboratory of Advanced Metal Materials for Special Environments, North University of China, Taiyuan 030051, China

ARTICLE INFO

Keywords:
High-entropy alloys
Flash annealing
Grain refinement
Martensitic transformation
Strength

ABSTRACT

High-entropy alloys (HEAs) have gained significant attention due to their exceptional properties, particularly dual-phase Fe-Mn-Co-Cr HEAs known for their transformation-induced plasticity (TRIP) and twinning-induced plasticity (TWIP) effects. Conventional slow annealing (SA) typically leads to grain coarsening, while flash Joule annealing (FJA) has emerged as an effective method for achieving grain refinement in conventional metals and alloys. In this work, both SA and FJA methods were employed to manipulate the microstructure and mechanical properties of dual-phase $Fe_{50}Mn_{30}Co_{10}Cr_{10}$ HEAs. It was revealed that the FJA-treated samples consistently demonstrate higher yield strength and ultimate tensile strength compared to the SA-treated and homogenized counterparts. Notably, at 1173 K, strength is enhanced with only a minimal decrease in total elongation. The enhanced yield strength can be attributed to grain refinement, variations in the austenitic-to-martensitic phase ratio, and heterogeneous grain and phase distributions. Furthermore, the plastic deformation behavior is governed by a combination of dislocation proliferation, TRIP, and TWIP effects, with their relative contributions varying under different annealing conditions. Our findings indicate the FJA as a promising strategy for achieving grain refinement and tailoring heterostructure in TRIP-type HEAs, thereby enhancing overall mechanical performance.

1. Introduction

In recent years, high-entropy alloys (HEAs) have gained considerable attention as a novel class of high-performance metallic materials due to their unprecedented compositional attributes and exceptional mechanical performance [1–6]. Compared to conventional metals and alloys, HEAs are characterized by multi-principal element configurations, which allows for wide-ranging adjustments in compositional design and promotes a paradigm shift in microstructural configuration [1–6]. The concept of HEAs also gives rise to several effects, including the high-entropy effect, lattice distortion effect, sluggish diffusion effect, and cocktail effect, which contributes to superior mechanical properties, high-temperature stability, corrosion resistance, and radiation tolerance [1–11]. Consequently, HEAs have been regarded as promising candidates for next-generation materials so far. However, like conventional metals and alloys, HEAs also encounter the challenge of the strength-ductility trade-off [6–9,12]. To enhance the strength of these materials, various alloy design strategies have been explored [6–9,12]. One efficient approach is modulating the stacking fault energy (SFE) of alloys [13]. Specifically, reducing the SFE to a critical value tends to promote mechanical twinning or martensitic transformation, inducing twinning-induced plasticity (TWIP) or transformation-induced plasticity (TRIP) effects, respectively [14–16]. Li et al. [16] first developed a dual-phase $Fe_{50}Mn_{30}Co_{10}Cr_{10}$ HEA with an advantageous combination of strength and ductility by adjusting the SFE. Subsequently, numerous studies have focused on this alloy system and its derivatives to explore

* Corresponding author at: School of Mechanical, Electrical & Information Engineering, Shandong University, Weihai 264209, China.
** Corresponding authors at: School of Materials Science and Engineering, North University of China, Taiyuan 030051, China.
E-mail addresses: zjyan@nuc.edu.cn (Z. Yan), songkaikai8297@gmail.com (K. Song).

https://doi.org/10.1016/j.jallcom.2025.182072
Received 4 October 2024; Received in revised form 2 July 2025; Accepted 3 July 2025
Available online 5 July 2025

their comprehensive performance [16–18]. However, achieving desirable structural features in these HEAs requires complex and time-consuming thermomechanical processing, such as hot forging, cold rolling, and annealing [16–19]. Therefore, developing a fast and effective method to enhance their mechanical properties is highly desirable.

To date, flash annealing has emerged as an approach to refine microstructures in various steel types, such as dual-phase steels [20], TRIP steels [21], and quenching and partitioning steels [22]. Hence, the flash annealing method is expected to be an efficient approach for the rapid enhancement of the mechanical properties of HEAs. Unlike conventional slow annealing (SA) methods, the flash annealing approach involves high heating rates of 100 K/s to 300 K/s, making it a promising approach for enhancing alloy performance while minimizing energy consumption and optimizing processing efficiency [23,24]. Initial investigations into the application the flash annealing processing in cold-rolled ultra-low carbon steels have the potential to hinder recrystallization and trigger explosive nucleation of austenite grains, resulting in significant grain refinement [25]. Although the flash annealing method has been applied to conventional metals and alloys, its potential suitability when used with HEAs needs further elucidation. Recently, our group has developed an innovative ultrafast annealing-deep cryogenic treatment-tempering method, which significantly enhances the mechanical properties of the as-cast $Fe_{50}Mn_{30}Co_{10}Cr_{10}$ HEA [15]. To further optimize material performance, it is essential to systematically investigate the relationship between microstructural modifications and mechanical properties induced by flash annealing alone, thereby establishing a foundation for maximizing its utility in advanced material design. In this study, we performed Flash Joule annealing (FJA), one of the most well-known flash annealing techniques, on the cold-rolled $Fe_{50}Mn_{30}Co_{10}Cr_{10}$ dual-phase HEA to verify the feasibility of the FJA method. The corresponding microstructure evolution and mechanical properties upon annealing at different temperatures were investigated in detail.

2. Experimental section

Ten button ingots with a nominal composition of $Fe_{50}Mn_{30}Co_{10}Cr_{10}$ were produced through arc melting under an argon atmosphere using pure metals with a purity greater than 99.9 wt%. To ensure chemical homogeneity, each ingot was remelted at least five times. Subsequently, all ingots were remelted in a high-frequency induction furnace under an argon protective atmosphere and cast into a plate with a dimension of 60 × 30 × 30 mm using a tilting casting method. The obtained plate underwent wire electric discharge machining to produce multiple plates with dimensions of 60 × 10 × 2 mm. The thermomechanical processing steps applied to these HEA plates are illustrated in Fig. S1 in the supplementary materials. As shown in Fig. S1, these plates were first homogenized at 1473 K for 24 h in an argon atmosphere, followed by water quenching. Cold-rolling was then performed on these homogenized plates to achieve a thickness reduction of ~45 %. Subsequently, the specimens were annealed at temperatures of 973 K and 1173 K for 30 s at different heating rates (i.e., 100 K/s and 0.167 K/s, Fig. S1), respectively. Among them, specimens heated at a heating rate of 100 K/s were processed using a thermomechanical simulator (Gleeble-3500C, DSI) and cooled using an Argon inert gas shower, referred to as the FJA sample. It is important to note that the thermomechanical simulator cannot uniformly heat the entire sample. To address this, flat dog-bone-shaped FJA samples (5 × 1.1 × 30 mm) are used during rapid heating. Specimens are then extracted from the central region, where temperature uniformity is confirmed via thermocouples, for subsequent microstructure characterization and mechanical testing. Specimens heated at a heating rate of 0.167 K/s were fabricated using a muffle furnace (KSL-1400X, Hefei Kejing) and then water quenched, referred to as the SA-treated sample. It should be mentioned that the applied cooling rate is quite higher for the SA-treated sample compared to the FJA-treated sample. To investigate the phenomenon of the reverse martensitic transformation during annealing, we subjected cold-rolled samples to the same annealing treatments at 673 K. The resulting samples were designated as SA673 and FJA673, corresponding to the SA and FJA methods, respectively.

To observe microstructural features, a ZEISS Sigma500 scanning electron microscope (SEM) equipped with an Oxford Nordlys max^3 electron backscatter diffraction (EBSD) was employed. The data were post-processed by Channel 5 and AZtecCrystal software, and GND density was also derived. Tensile testing was conducted using a SUNS UTM5015 electronic tensile testing machine at an initial strain rate of 5×10^{-4} s^{-1}. The localized strain distributions during tension were observed using an IMETRUM PCA1200 digital image correlation (DIC) method. Flat dog-bone-shaped specimens with a dimension of 2.5 × 1.1 × 6 mm were prepared for tensile tests. To ensure the reliability and repeatability, three tests were repeated for each sample.

3. Results and discussion

3.1. Microstructure features of the SA973 and FJA973 samples

The microstructure characteristics of the SA973 and FJA973 samples are illustrated in Figs. 1 and 2. As shown in Fig. 1(a), the band contrast map (BC) reveals the presence of numerous deformed structures in the SA973 sample, indicating partial recrystallization following the SA treatment. As evidenced by Fig. 1(a) and (b), the average grain size of the SA973 sample is measured to be ~ 4.56 μm (Table S1), with a notably heterogeneous grain size distribution (Fig. 1(c)). Coarse grains (> 5 μm) account for approximately 13.8 % in number fraction and 68.6 % in area fraction, while fine grains (≤ 5 μm) constitute about 86.2 % and 31.4 %, respectively (Fig. 1 and Table S1). As displayed in Fig. 1(d), the SA973 sample is composed of face-centered cubic (FCC) and hexagonal close-packed (HCP) phases. Both phases exhibit equiaxed grains spanning from fine to coarse dimensions (Fig. 1(e) and (f)), with average grain sizes of ~4.51 μm for FCC and ~4.63 μm for HCP grains. FCC grains constitute approximately 56.3 % in number fraction and 52.3 % in area fraction, while HCP grains account for roughly 43.7 % and 47.7 %, respectively (Table S1). For the FCC phase, coarse grains constitute about 13.5 % in number fraction and 76.6 % in area fraction, with fine grains making up ~86.2 % and ~23.4 %. For the HCP phase, coarse grains represent approximately 25.1 % in number fraction and 92.2 % in area fraction, while fine grains account for ~74.9 % and ~7.8 % (Table S1 and Fig. 1(e) and (f)). As depicted in Fig. 1(g) and (h), grain boundary characterization distinguishes between high-angle grain boundaries (HAGBs, $\theta \geq 15°$) and low-angle grain boundaries (LAGBs, $2° \leq \theta \leq 15°$). HAGBs are marked by red and blue lines for FCC and HCP phases, respectively, while LAGBs are indicated by green and purple lines. Overall, HAGBs account for about 50.4 % of the grain boundaries, and LAGBs for approximately 49.6 % (Fig. 1(i) and Table S1), indicating the substantial formation of fine grains during annealing [26,27]. Specifically, HAGBs constitute around 39.6 % of FCC grains and 64.3 % of HCP grains, whereas LAGBs make up about 60.4 % of FCC grains and ~35.7 % of HCP grains (Fig. 1(i) and Table S1).

In contrast, the FJA973 sample, as illustrated in Fig. 2, exhibits a finer microstructure compared to the SA973 sample, with an average grain size of approximately 3.73 μm (Table S1 and Fig. 2(a) and (d))). Coarse grains (> 5 μm) account for approximately 16.3 % in number fraction and 63 % in area fraction, while fine grains (≤ 5 μm) constitute about 83.7 % and 37 %, respectively (Fig. 2(c) and Table S1). Similar to the SA973 sample, the FJA973 sample comprises FCC and HCP phases with heterogeneous grain distributions (Fig. 2(d–f)). The average grain sizes are approximately 3.43 μm for FCC and 4.06 μm for HCP, both smaller than those in the SA973 sample. FCC grains represent approximately 46.9 % in number fraction and 48.8 % in area fraction, while HCP grains account for roughly 53.1 % and 51.2 %, respectively. For the FCC phase, coarse grains constitute about 19.8 % in number fraction and 64.7 % in area fraction, with fine grains making up ~80.2 % and ~35.3 %. In the HCP phase, coarse grains represent approximately

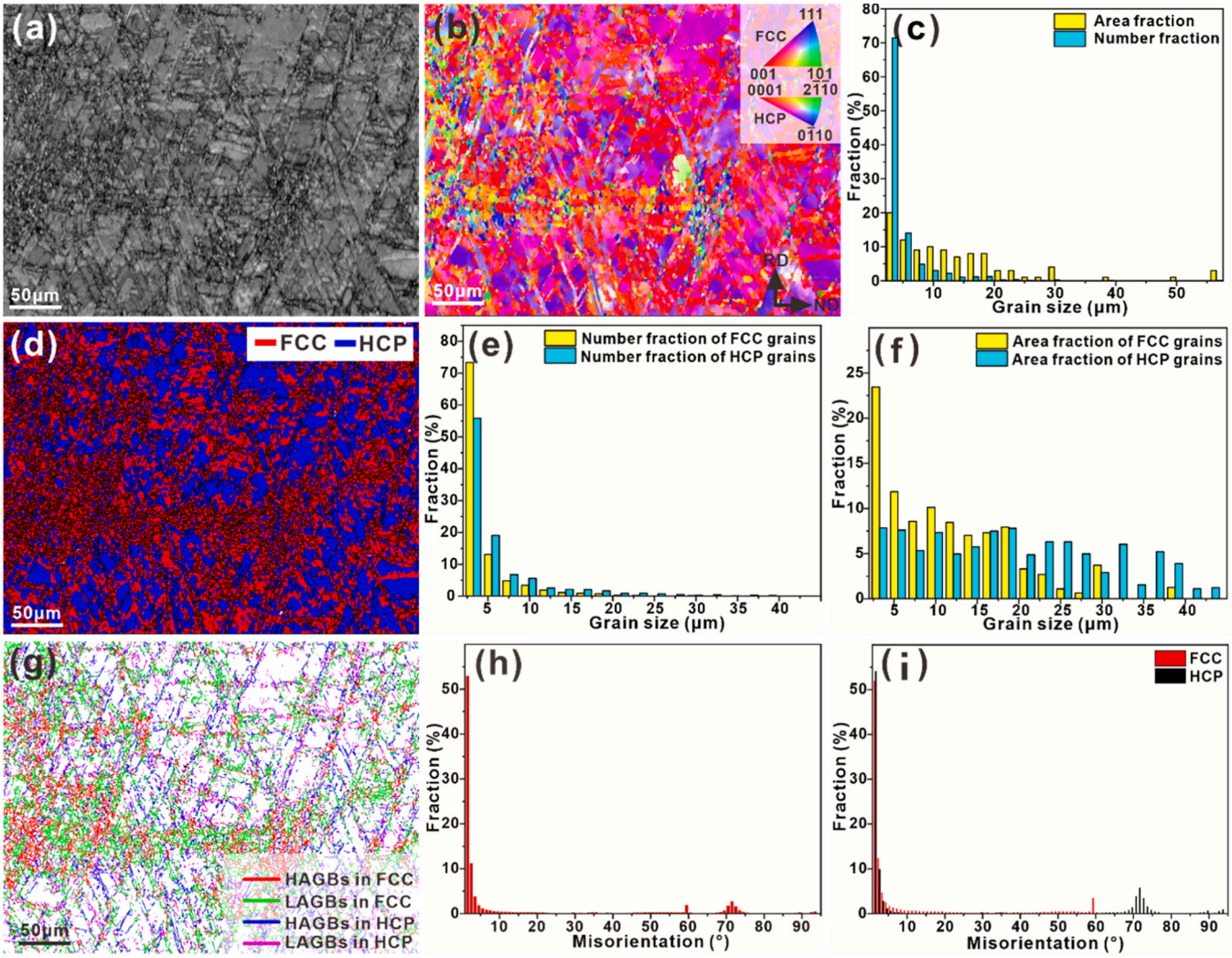

Fig. 1. Microstructure features of the SA973 sample. (a) BC map, (b) inverse pole figure (IPF), (c) grain size distributions of all grains, (d) phase map, (e) number and (f) area fractions of both FCC and HCP grains, (g) grain boundary map, (h) misorientation distributions of all grains, and (i) misorientation distributions of both FCC and HCP grains.

19.1 % in number fraction and 65.0 % in area fraction, while fine grains account for ~80.8 % and ~35.0 % (Table S1 and Fig. 2(e) and (f)). Grain boundary distribution of the FJA973 sample in Fig. 2(g) and (h) reveals that HAGBs account for approximately 51.2 % of the boundaries, and LAGBs for about 48.8 % (Table S1). Specifically, HAGBs constitute around 49.9 % of FCC grains and 50.5 % of HCP grains, whereas LAGBs make up approximately 50.1 % of FCC grains and 49.5 % of HCP grains (Fig. 2(i) and Table S1). In summary, the SA973 sample exhibits a heterogeneous distribution of grain sizes and phases, with a substantial presence of fine grains and a notable fraction of HAGBs, particularly in the HCP phase. In contrast, the FJA973 sample demonstrates a finer microstructure, a higher fraction of HCP grains, and a more pronounced heterogeneity in the distribution of phases and grain sizes.

3.2. *Microstructure features of the SA1173 and FJA1173 samples*

The microstructural features of the SA1173 and SA1173 samples are depicted in Figs. 3 and 4. The BC map in Fig. 3(a) reveals minimal deformation from cold rolling, indicating complete recrystallization in the SA973 sample. EBSD analysis shows an average grain size of approximately 4.41 μm (Fig. 3(a) and (b)). Fine grains (≤ 5 μm) account for about 78.4 % of the number fraction and 37.4 % of the area fraction (Table S1 and Fig. 3(c)). The phase map in Fig. 3(d) and the grain size distributions in Fig. 3(e) and (f) demonstrate that the SA1173 sample consists of FCC and HCP phases. FCC grains represent approximately 43.3 % in number fraction and 37.6 % in area fraction, while HCP grains account for about 56.7 % and 62.4 %, respectively. The average grain sizes for the FCC and HCP phases are approximately 4.45 μm and 4.38 μm, respectively (Table S1). In the FCC phase, fine grains comprise roughly 71.8 % of the total grain count but only 30.2 % of the total area, whereas coarse grains (>5 μm) account for approximately 28.2 % of the grain count and 69.8 % of the area. Similarly, in the HCP phase, fine grains make up about 76.9 % of the grain count and 33.6 % of the area, while coarse grains represent around 23.1 % of the grain count and 66.4 % of the area (Table S1 and Fig. 3(e-f)). Grain boundary characterization (Fig. 3(g)) shows a predominance of HAGBs, which account for about 93.9 % of the boundaries, while LAGBs make up approximately 6.1 % (Fig. 3(h) and Table S1). Specifically, HAGBs represent ~92.2 % of FCC grains and ~94.9 % of HCP grains, whereas LAGBs make up approximately 7.8 % of FCC grains and ~5.1 % of HCP grains (Fig. 3(i) and Table S1).

On the other hand, the microstructure of the FJA1173 sample shows a finer grain size compared to the SA1173 sample (Fig. 4(a-d)). The average grain size of the FJA1173 sample is approximately 3.52 μm, with average grain sizes of ~2.95 μm for the FCC phase and ~3.72 μm for the HCP phase (Fig. 4(e) and (f)). This refinement is attributed to the

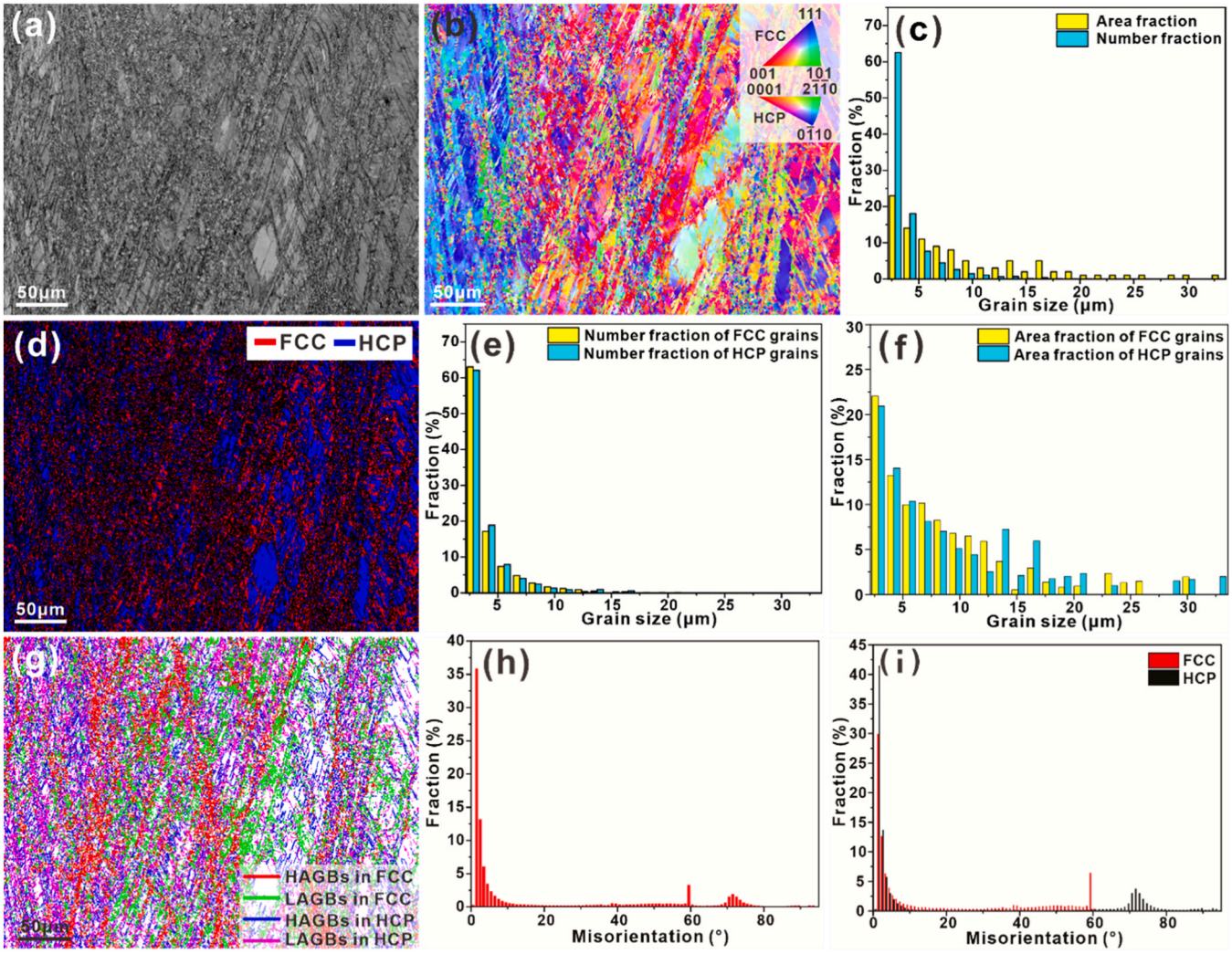

Fig. 2. Microstructure features of the FJA973 sample. (a) BC map, (b) IPF, (c) grain size distributions of all grains, (d) phase map, (e) number and (f) area fractions of both FCC and HCP grains, (g) grain boundary map, (h) misorientation distributions of all grains, and (i) misorientation distributions of both FCC and HCP grains.

inhibition of grain coarsening by the short annealing time during the FJA treatment. The phase map (Fig. 4(d)) reveals that the FJA1173 sample has a significantly higher volume fraction of the HCP phase (~78.5 %) compared to the SA1173 sample (~56.7 %). Similar to the SA1173 sample, the grain boundary map and misorientation distributions (Fig. 4(g-i)) demonstrate that the FJA1173 sample is predominantly composed of HAGBs, further confirming the refined microstructure and complete recrystallization. All in all, the SA1173 sample still exhibits a heterogeneous phase distribution with a high proportion of HAGBs, indicating complete recrystallization. However, significant heterogeneity in grain size is not observed due to annealing at relatively higher temperatures. In contrast, the FJA1173 sample demonstrates a finer grain size, a higher fraction of the HCP phase, and a more refined microstructure due to the short annealing time during the FJA treatment. These findings highlight the significant influence of different annealing conditions on microstructural evolution.

3.3. Structural origin of the SA- and FJA-treated samples

The present study demonstrates that the FJA treatment can effectively induce grain refinement and tailor heterogeneous grain and phase distributions [28,29], thereby enhancing the mechanical properties of TRIP-type HEAs. The microstructure of the present HEAs is predominantly martensite due to mechanical deformation after homogenization and cold rolling. It has been reported that the inverse martensitic transformation temperature of these HEAs is approximately 403 K [30]. As illustrated in Fig. 5, annealing at 673 K using both the SA and FJA methods results in no significant static recrystallization for either sample. Under the SA condition, approximately 95 % FCC austenite is observed, while the FJA method achieves about 75 % FCC austenite. This indicates that heating induces the inverse martensitic transformation, leading to the formation of FCC austenite. Cold rolling introduces dislocations and other defects into the martensite structure, acting as barriers to phase boundary movement and hindering the transformation back to austenite [31,32]. This phenomenon, known as the mechanical stabilization of martensite, prevents significant static recrystallization upon heating at 673 K, leaving the stored plastic deformation or stress unreleased and resulting in retained martensite. Upon cooling, the martensitic transformation occurs again, but the transformation temperature is significantly lower than the inverse martensitic transformation temperature. Additionally, cold rolling-induced plastic deformation or stress causes a more gradual transformation over a wider temperature range [33,34]. Consequently, the martensitic transformation temperature of the cold-rolled sample is well below 403 K, nearing room temperature. Therefore, after both SA and FJA treatments at 673 K, the microstructure of the present HEAs remains predominantly austenite without pronounced martensitic transformation, and the retained martensite originates from the cold

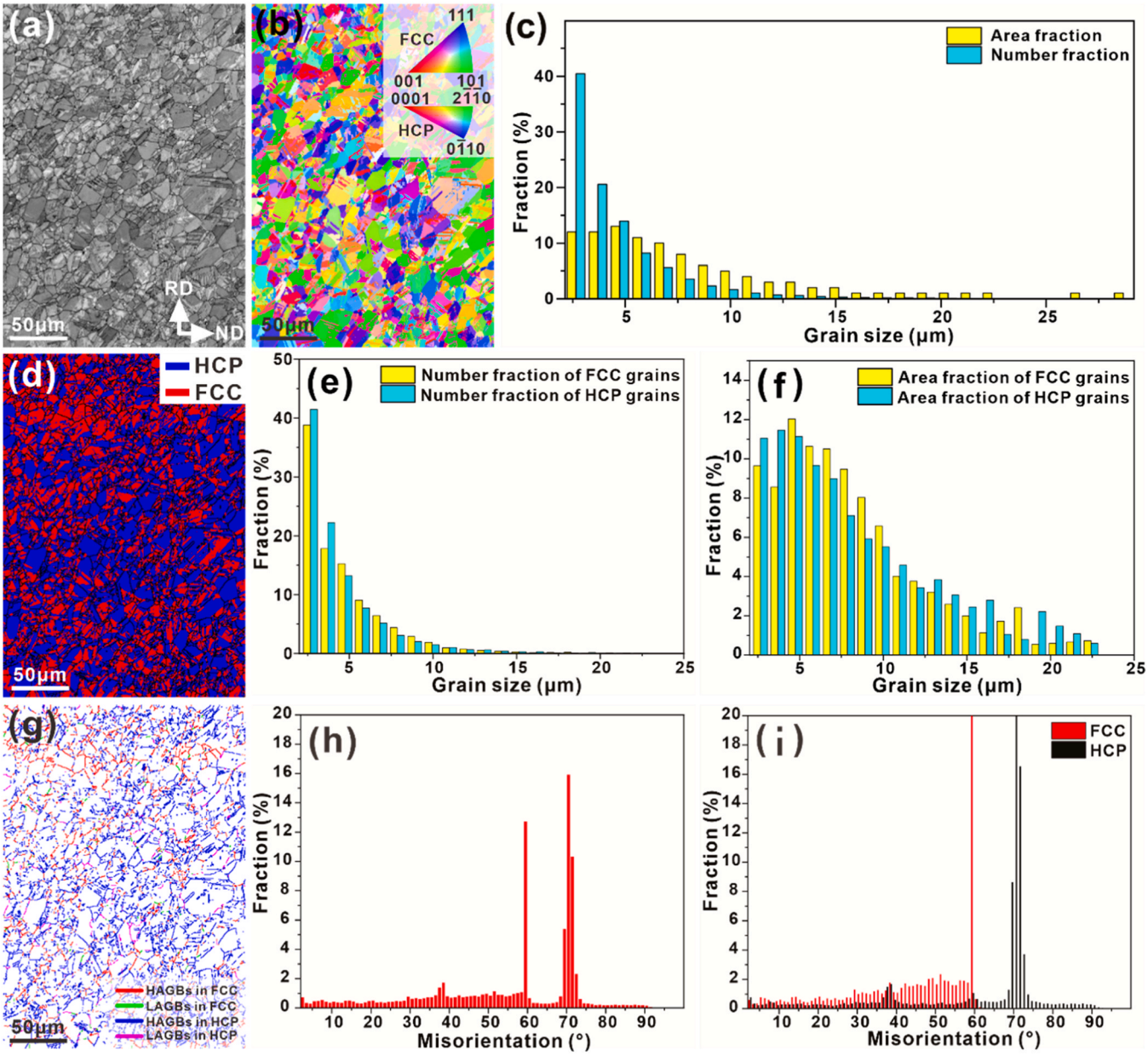

Fig. 3. Microstructure features of the SA1173 sample. (a) BC map, (b) IPF, (c) grain size distributions of all grains, (d) phase map, (e) number and (f) area fractions of both FCC and HCP grains, (g) grain boundary map, (h) misorientation distributions of all grains, and (i) misorientation distributions of both FCC and HCP grains.

rolling process. As a result, more retained martensite is observed in the FJA973 and FJA1173 samples because more plastic deformation or stress is released under the SA condition than the FJA condition, requiring more annealing time. Upon annealing at 973 K and 1173 K, as shown in Figs. 1–4, significant static recrystallization occurs. The degree of recrystallization increases, leading to a gradual decrease in average grain size and noticeable grain refinement of all annealed samples compared to the homogenized sample. Incomplete recrystallization typically leads to a heterogeneous grain distribution, particularly in samples annealed at 973 K, as confirmed by EBSD observations (Figs. 1–4). Due to the incomplete recrystallization and the short hold time of 30 s, many deformed grains remain in the samples annealed at 973 K, resulting in a slightly larger average grain size. When the annealing temperature increases to 1173 K, recrystallization nearly completes, and the growth of recrystallized grains is effectively inhibited due to the insufficient time for grain growth [35] by the short holding time and rapid cooling rate. Consequently, both samples annealed at 1173 K using the SA and FJA methods exhibit a finer microstructure than the homogenized sample. Furthermore, under the same temperature annealing conditions, the average grain size obtained by the FJA method is more heterogeneous in distribution and smaller than that achieved by the SA method. This difference can be attributed to the shorter duration of the FJA process compared to the SA process at the same temperature.

Moreover, as the annealing temperature increases, a higher proportion of HCP martensite is observed, accompanied by a significant decrease in FCC austenite content (Table S1). Interestingly, the average grain sizes of both FCC austenite and HCP martensite show a slight increase (Table S1), while the HCP martensite is larger than the FCC austenite. During recrystallization, the stored plastic deformation or stress is released, and induced defects such as dislocations, slip bands, and deformation bands are rearranged and eventually eliminated. This process allows for the formation of strain-free grains. The resulting finer grains after recrystallization provide numerous grain boundaries, some

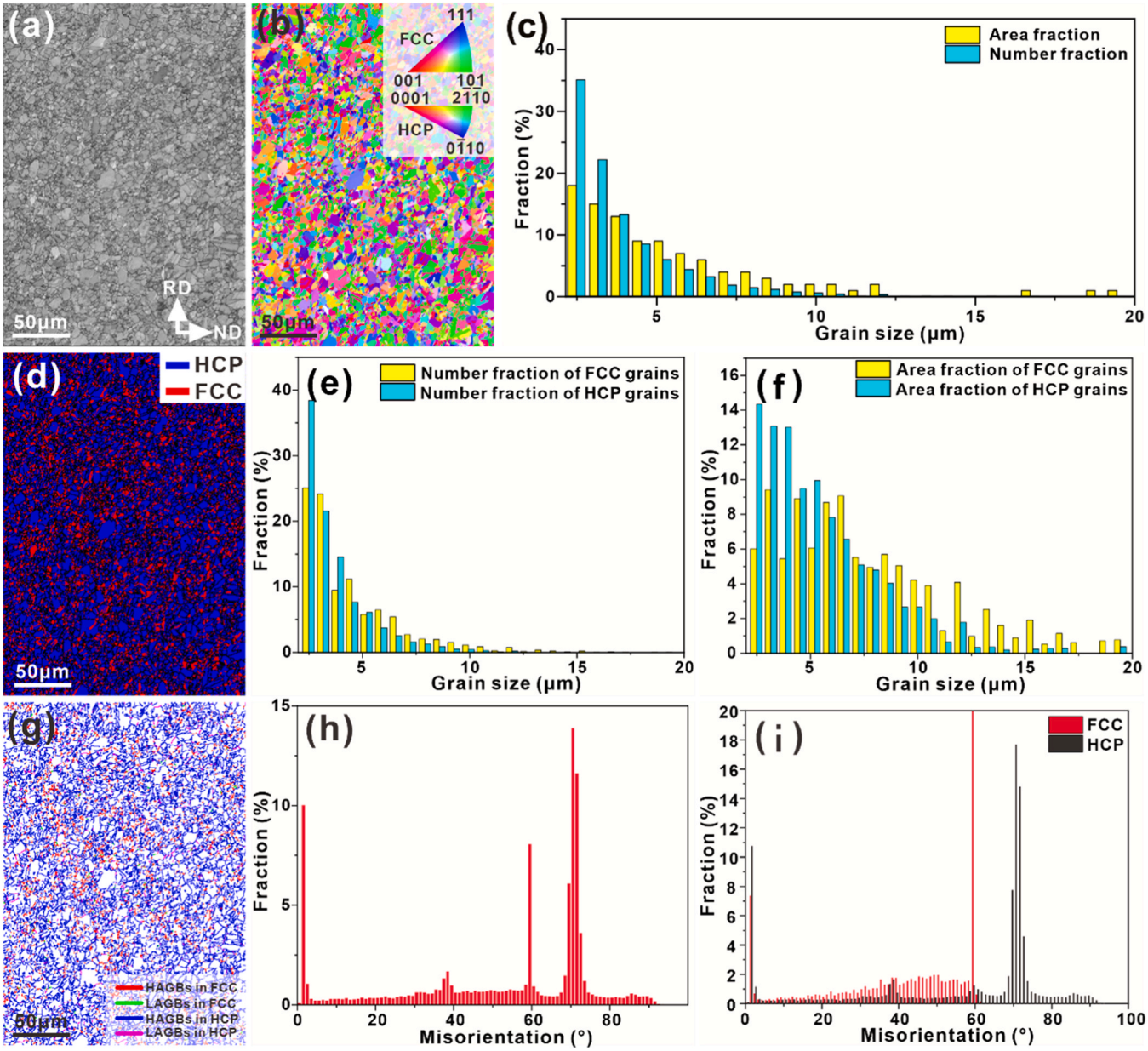

Fig. 4. Microstructure features of the FJA1173 sample. (a) BC map, (b) IPF, (c) grain size distributions of all grains, (d) phase map, (e) number and (f) area fractions of both FCC and HCP grains, (g) grain boundary map, (h) misorientation distributions of all grains, and (i) misorientation distributions of both FCC and HCP grains.

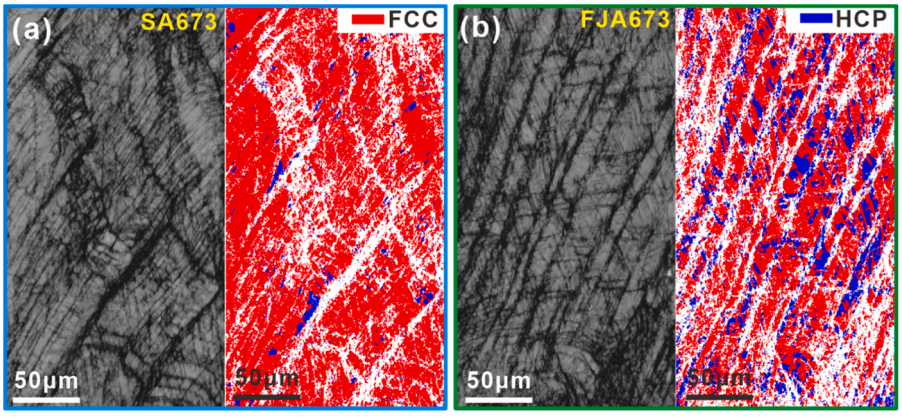

Fig. 5. BC and phase maps of the (a) SA673 and (b) FJA673 samples.

of which may serve as preferential nucleation sites for martensite during rapid cooling. Furthermore, the increase in annealing temperature leads to a higher phase transformation driving force, facilitating the activation of martensitic transformation. This results in enhanced nucleation and growth of martensite. However, as reported by Li et al. [36], grain refinement also can lead to higher resistance for martensite transformation, which results in the occurrence of incomplete martensite transformation. Consequently, in addition to heterogeneous grain distributions, the material also exhibits heterogeneous distributions of both FCC and HCP phases.

3.4. Mechanical properties of the SA1173 and FJA1173 samples

Fig. 6(a) exhibits the engineering stress-strain curve of the FJA- and SA-treated samples annealed at 973 K and 1173 K for 30 s, respectively. Compared to the SA-treated samples, the FJA-treated samples exhibit higher yield strength and ultimate tensile strength. Upon annealing at 973 K, the FJA973 sample shows the highest yield strength of 556 ± 27.8 MPa, which is ~51 % higher than the SA973 sample (i.e., 367.4 ± 18.4 MPa). The ultimate tensile strength (i.e., 857.2 ± 17.1 MPa) of the FJA973 sample is also higher than the SA973 sample (i.e., 802.6 ± 27.8 MPa). Yet, the SA973 sample displays a better elongation of ~26.7 % than the FJA973 sample (i.e., ~15.4 %). Obviously, annealing at 973 K reveals a significant difference in yield strength and ultimate tensile strength, confirming that the FJA method effectively strengthens the TRIP-type HEAs. Meanwhile, the corresponding true stress-strain curves and the strain-hardening rate curves are depicted in Fig. 6(b). The strain-hardening rate of the SA973 sample is higher than that of the FJA973 sample when beyond ~10 % elongation.

On the other hand, upon annealing at 1173 K, the FJA1173 sample also displays a higher yield strength of 267.1 ± 13.4 MPa and ultimate tensile strength of 821.7 ± 16.4 MPa compared to the SA1173 sample (yield strength: 252.0 ± 12.6 MPa and ultimate tensile strength: 695.4 ± 20.8 MPa), together with almost similar total elongation (Fig. 6(a)). As shown in Fig. 6(a), the total elongation (~42.8 %) of the FJA-treated sample is only ~2.4 % lower than that of the SA-treated sample (~45.2 %). Meanwhile, the strain-hardening rate of the FJA1173 sample is higher than that of the SA1173 sample after ~10 % elongation (Fig. 6(b)). Compared to the mechanical properties of previously reported dual-phase $Fe_{50}Mn_{30}Co_{10}Cr_{10}$ HEAs [7,16,18,37–43], the (yield) strength of the FJA-treated samples can match or surpass those fabricated through intricate and complex thermomechanical processes (Fig. 6 (c) and (d)).

3.5. Deformation mechanisms of the SA1173 and FJA1173 samples

For the dual-phase $Fe_{50}Mn_{30}Co_{10}Cr_{10}$ HEAs, the grain size and the fraction of the thermally-induced HCP grains are the main factors that affect the mechanical properties. On the one hand, the finer grain size will improve the yield strength of materials, which can be explained by the Hall-Petch effect [44,45]. Finer grains lead to an increase in the number of grain boundaries that can act as barriers to dislocation

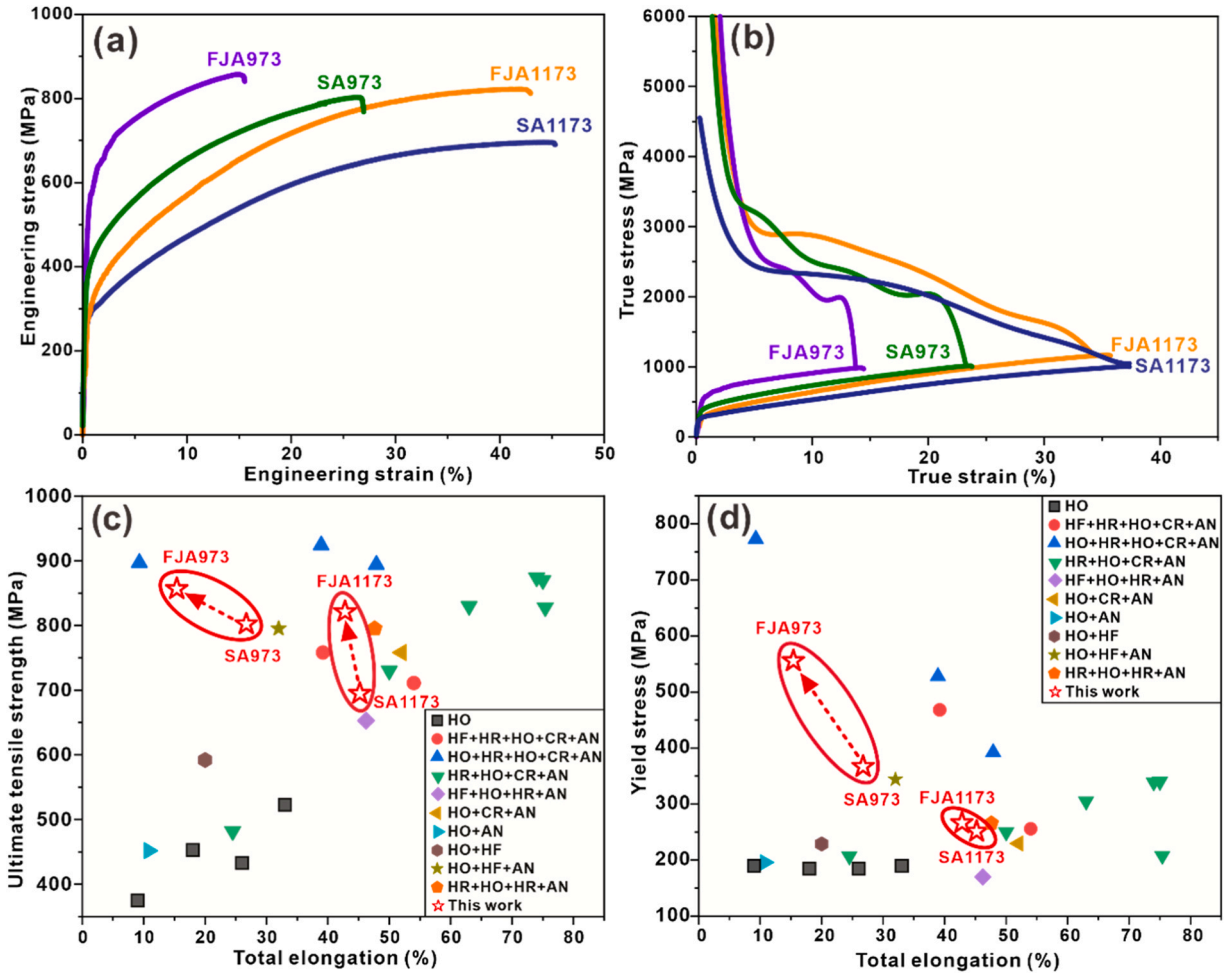

Fig. 6. (a) Engineering stress-strain curves of the samples annealed at 973 K and 1173 K, (b) true stress-strain curves superimposed with corresponding strain hardening curves, (c) total elongation *vs.* ultimate tensile strength and (d) total elongation *vs.* yield strength of reported $Fe_{50}Mn_{30}Co_{10}Cr_{10}$ HEAs by different methods (HF, HR, HO, CR, and AN represent hot forging, hot rolling, homogenization, cold rolling, and annealing, respectively) [7,16,18,37–43] as well as our observations.

movement, thereby increasing the strength. On the other hand, the HCP phase is harder than the FCC phase and less deformable [46], so the increased fraction of initial HCP grains can improve the yield strength and tensile strength but often damage the ductility of materials [47,48]. Furthermore, the smaller the grain size, the higher the number of nucleation sites, which can enhance the phase transformation kinetics and then ensure the strain hardening capability and ductility. Compared to the SA-treated samples, the FJA-treated samples exhibit finer microstructures, but slightly fewer HCP grains. In addition, all samples exhibit significant heterogeneity in both grain size and phase distribution, which also leads to stress and strain partitioning during deformation. This heterogeneous microstructure creates a complex stress state within the materials during deformation. Softer regions tend to deform more readily, while harder regions resist deformation. This disparity in deformation behavior results in the development of long-range internal stresses, contributing to the overall back stress in the materials [49]. All in all, the interplay of these factors, i.e., finer microstructure, increased HCP grain content, and heterogeneous grain and phase distributions, collectively contributes to the higher yield strength observed in all annealed samples compared to the homogenized sample.

To further illustrate the plastic deformation behaviors of the annealed samples under the SA and FJA conditions, we examined the microstructural features of the SA973, SA1173, FJA973, and FJA1173 samples after fracture (Figs. 7 and 8). Fig. 7 reveals severe plastic deformation in both SA973 and FJA973 samples (Fig. 7(a) and (b)), making some areas unrecognizable by EBSD. The microstructures predominantly consist of martensite phases (Fig. 7(c) and (d)). Specifically, the deformed SA973 sample contains approximately 4.3 % FCC phase, while the deformed FJA973 sample contains around 0.9 % FCC phase, indicating a widespread TRIP effect during plastic deformation. Furthermore, KAM maps demonstrate a higher density of dislocations in the severely deformed zones compared to the coarse HCP grains (Fig. 7 (e) and (f)), suggesting significant dislocation proliferation during plastic deformation. In both cases, dislocations activate in the softer fine and coarse FCC grain regions, initiating their transformation into martensite during the early stage of the plastic deformation. Meanwhile, pre-existing coarse martensite grains remain in an elastic state. As deformation progresses and martensite becomes dominant, plastic deformation begins in the martensitic phase. The heterogeneous distribution of martensite leads to different deformation behaviors. Fine martensite grains resist plastic deformation more than their coarse counterparts, resulting in dislocation entanglement within the latter.

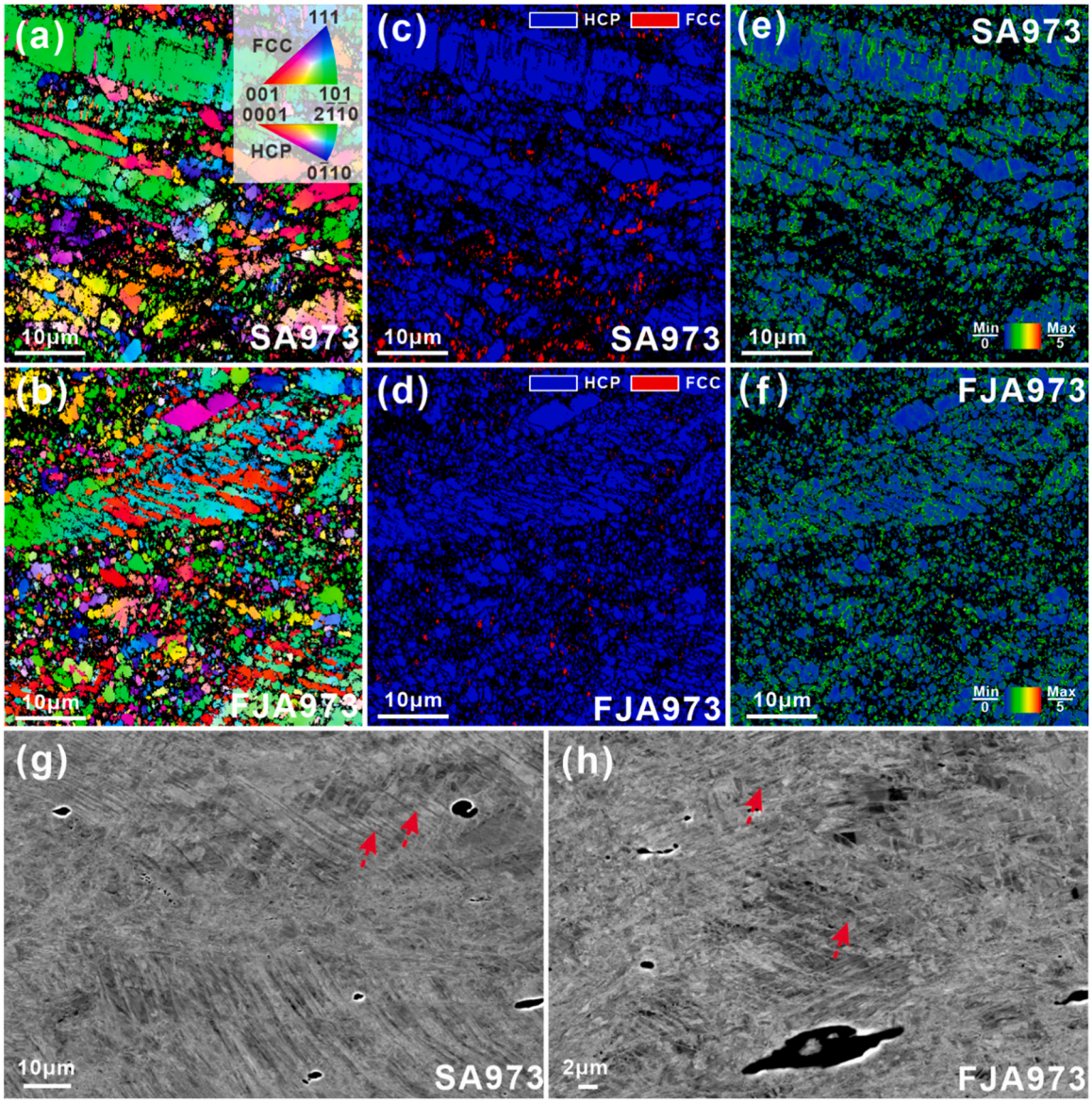

Fig. 7. EBSD and SEM observations of the SA973 and FJA973 samples after fracture: (a,d) IPF maps, (c,d) phase maps, (e,f) KAM maps, and (g,h) SEM images.

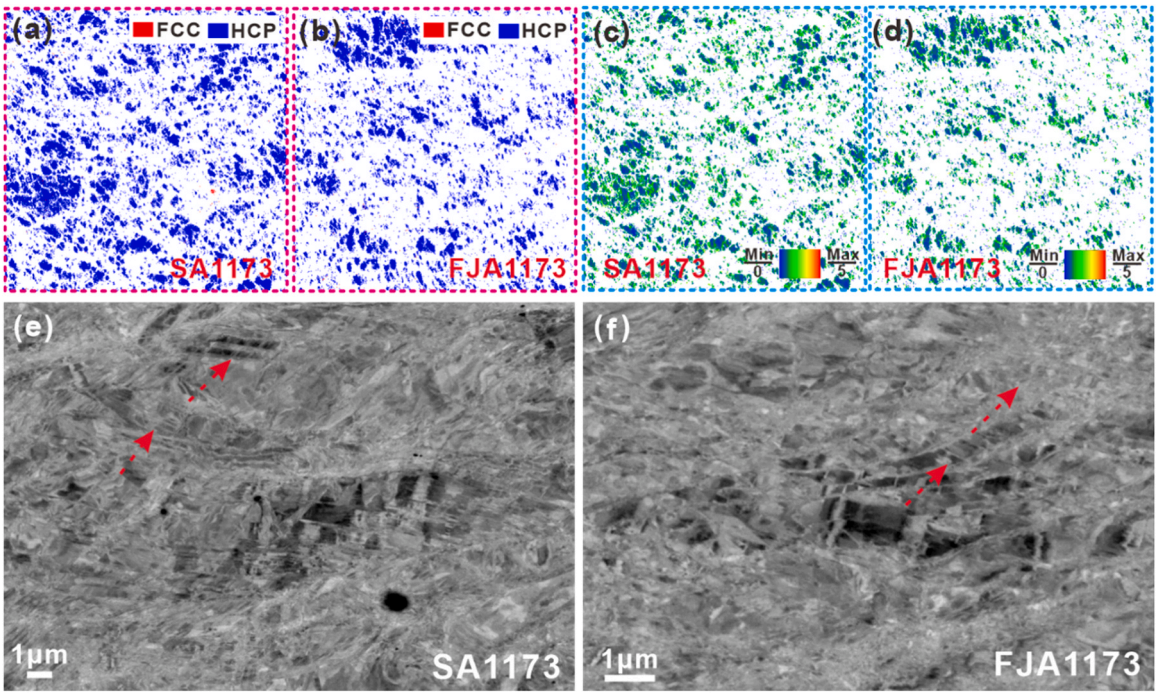

Fig. 8. Microstructural features of the SA1173 and FJA1173 samples after fracture. (a,b) phase maps, (c,d) KAM maps, and (e,f) SEM images.

These dislocations in coarse grain regions generate long-range back stresses, inhibiting further dislocation emission. Consequently, dislocation proliferation concentrates at the edges of coarse-grained regions near fracture (Fig. 7(e) and (f)). In addition to dislocation motion, deformation twins emerge (indicated by red dotted arrows in Fig. 7(g) and (h)), contributing to the strength. The SA973 sample, with more pre-existing austenite, exhibits larger strain-hardening rates during plastic deformation compared to the FJA973 sample. As a result, the FJA973 sample shows higher yield strength but less tensile plastic strain, with plastic deformation primarily driven by dislocation proliferation and the TRIP effect. On the other hand, similar structural evolution is observed in the SA1173 and FJA1173 samples after fracture (Fig. 8). These samples initially contain substantial pre-existing martensite. Post-deformation phase mapping reveals predominantly the HCP phase, with the FCC phase barely detectable (Fig. 8(a) and (b)). Numerous slip bands and dislocations are evident in the deformed grains (Fig. 8(c–f)). Notably, both samples display significant deformation twinning (red dotted arrows in Fig. 8(e) and (f)), indicating that dislocation proliferation, TRIP, and TWIP effects collectively govern the plastic deformation of both samples.

4. Conclusions

The current study investigates the effects of both the SA and FJA methods on the microstructure and mechanical properties of transformation-induced plasticity (TRIP)-type $Fe_{50}Mn_{30}Co_{10}Cr_{10}$ HEAs. The FJA samples exhibit significantly higher yield and tensile strengths than the SA-treated samples, especially notable at 973 K, where the FJA samples show a ~51 % increase in yield strength. However, the SA-treated samples demonstrate better elongation. At 1173 K, the FJA samples still outperform SA in strength while maintaining comparable elongation. The cold rolling process significantly influences microstructural evolution by introducing dislocations that inhibit grain growth and increase retained martensite, especially in the FJA-treated samples. This is due to greater plastic deformation or stress release under the SA conditions, requiring longer annealing times than the FJA. Compared to the SA-treated samples, the FJA-treated samples exhibit more heterogeneous grain and phase distributions as well as grain refinement due to shorter processing times and recrystallization, resulting in the enhancement of yield strength. Post-deformation analysis shows significant deformation twinning, with phase mapping indicating predominant HCP phases and minimal FCC phases, driven by dislocation proliferation, TRIP, and TWIP effects. Thus, the FJA effectively induces grain refinement and enhances mechanical properties in TRIP-type HEAs, highlighting the critical role of processing conditions in advanced HEAs.

CRediT authorship contribution statement

Xiaoliang Han: Investigation, Formal analysis. **Kaikai Song:** Writing – review & editing, Supervision, Funding acquisition, Conceptualization. **Jianhong Gong:** Writing – review & editing, Formal analysis. **Pingping Liu:** Methodology, Formal analysis. **Changshan Zhou:** Writing – original draft, Methodology, Investigation, Data curation. **Qingwei Gao:** Methodology, Investigation. **Zhijie Yan:** Writing – review & editing, Writing – original draft, Data curation. **Jiyao Zhang:** Methodology, Formal analysis. **Xiqiang Wang:** Methodology, Investigation.

Declaration of Competing Interest

The authors declare that they have no known competing financial interests or personal relationships that could have appeared to influence the work reported in this paper.

Acknowledgements

The authors are grateful to K. Wang and Y. Xin from the Physical-Chemical Materials Analytical & Testing Center of Shandong University at Weihai for technical assistance. This work is supported by the Opening Foundation of Shanxi Key Laboratory of Advanced Metal Materials for Special Environments (AMMSE-2023-001), the Natural Science Foundation of Shandong Province (ZR2023ME216), and the National Natural Science Foundation of China (52471138).

Appendix A. Supporting information

Supplementary data associated with this article can be found in the online version at doi:10.1016/j.jallcom.2025.182072.

Data availability

Data will be made available on request.

References

[1] S.S. Nene, S. Sinha, D.K. Yadav, A. Dutta, Metallurgical aspects of high entropy alloys, J. Alloy. Compd. 1005 (2024) 175849.
[2] B. Cantor, Multicomponent high-entropy Cantor alloys, Prog. Mater. Sci. 120 (2021) 100754.
[3] D. Kumar, R. Seetharam, K. Ponappa, A review on microstructures, mechanical properties and processing of high entropy alloys reinforced composite materials, J. Alloy. Compd. 972 (2024) 172732.
[4] J. Chen, X. Zhou, W. Wang, B. Liu, Y. Lv, W. Yang, D. Xu, Y. Liu, A review on fundamental of high entropy alloys with promising high–temperature properties, J. Alloy. Compd. 760 (2018) 15–30.
[5] Y. Qiu, S. Thomas, M.A. Gibson, H.L. Fraser, N. Birbilis, Corrosion of high entropy alloys, npj Mater. Degrad. 1 (2017) 15.
[6] Q. Gao, Z. Kou, C. Zhou, X. Liu, J. Zhang, J. Gong, K. Song, L. Hu, Z. Liu, Z. Zhang, J. Eckert, R.O. Ritchie, Exceptional strength-ductility synergy in a casting multi-principal element alloy with a hierarchically heterogeneous structure, Mater. Today 81 (2024) 70–83.
[7] Z. Li, C.C. Tasan, K.G. Pradeep, D. Raabe, A. TRIP-assisted, dual-phase high-entropy alloy: grain size and phase fraction effects on deformation behavior, Acta Mater. 131 (2017) 323–335.
[8] S. Liu, T. Sun, Z. Kou, X. Han, Q. Gao, J. Zhang, X. Liu, L.C. Zhang, J. Orava, K. Song, L. Xiao, J. Eckert, W. Song, Promising pathways for balancing strength and ductility in chemically complex alloys with medium-to-high stacking fault energies, Int. J. Plast. 190 (2025) 104358.
[9] Z. Cui, D. Si, J. Zhang, Q. Gao, J. Gong, X. Wang, K. Song, X. Han, K. Zhang, Y. Mu, Y. Jia, D. Şopu, Z. Zhang, P. Ramasamy, J. Qiao, W. Song, G. Wang, L. Zhang, J. Eckert, Advancing the mechanical performance of chemically complex alloys through strategically engineered bamboo-inspired multi-stage heterostructures, Compos. Part B-Eng. 302 (2025) 112547.
[10] A. Hussain, R.S. Dhaka, H.J. Ryu, S.K. Sharma, P.K. Kulriya, A critical review on temperature dependent irradiation response of high entropy alloys, J. Alloy. Compd. 948 (2023) 169624.
[11] J. Liu, Z. Lv, Z. Wu, J. Zhang, C. Zheng, C. Chen, D. Ju, L. Che, Research progress on the influence of alloying elements on the corrosion resistance of high-entropy alloys, J. Alloy. Compd. 1002 (2024) 175394.
[12] X. Liu, K. Song, Z. Kou, J. Gong, X. Chen, Q. Gao, H. Sun, P. Liu, R. Qu, L. Hu, Z. Zhang, P. Ramasamy, Z. Liu, Z. Zhang, F. Liu, Z. Zhang, J. Eckert, Synergistic grain boundary engineering for achieving strength-ductility balance in ultrafine-grained high-Cr-bearing multicomponent alloys, Int. J. Plast. 177 (2024) 103992.
[13] M.J. Mills, T. Neeraj, Dislocations in metals and metallic alloys, in: K.H.J. Buschow, R.W. Cahn, M.C. Flemings, B. Ilschner, E.J. Kramer, S. Mahajan, P. Veyssière (Eds.), Encyclopedia of Materials: Science and Technology, Elsevier, Oxford, 2001, pp. 2278–2291.
[14] S. Curtze, V.T. Kuokkala, Dependence of tensile deformation behavior of TWIP steels on stacking fault energy, temperature and strain rate, Acta Mater. 58 (2010) 5129–5141.
[15] C. Zhou, Z. Kou, K. Song, J. Gong, P. Liu, Q. Gao, X. Liu, X. Han, Z. Zhang, P. Ramasamy, L. Hu, J. Orava, J. Eckert, Evading strength-ductility trade-off dilemma in TRIP-assisted Fe50Mn30Co10Cr10 duplex high-entropy alloys via flash annealing and deep cryogenic treatments, Acta Mater. 268 (2024) 119779.
[16] Z. Li, K.G. Pradeep, Y. Deng, D. Raabe, C.C. Tasan, Metastable high-entropy dual-phase alloys overcome the strength-ductility trade-off, Nature 534 (2016) 227–230.
[17] A. Tajik, A. Zarei-Hanzaki, H.R. Abedi, A. Moshiri, G. Lee, S.S. Sohn, Substructure development, martensitic transformation and rapid work-hardening in an as-cast interstitial substituted N atom in FeMnCoCr high-entropy alloy, J. Alloy. Compd. 960 (2023) 170705.
[18] Z. He, N. Jia, H. Yan, Y. Shen, M. Zhu, X. Guan, X. Zhao, S. Jin, G. Sha, Y. Zhu, C. T. Liu, Multi-heterostructure and mechanical properties of N-doped FeMnCoCr high entropy alloy, Int. J. Plast. 139 (2021) 102965.
[19] Z.F. He, N. Jia, H.W. Wang, Y. Liu, D.Y. Li, Y.F. Shen, The effect of strain rate on mechanical properties and microstructure of a metastable FeMnCoCr high entropy alloy, Mater. Sci. Eng. A 776 (2020) 138982.
[20] X. Wan, G. Liu, Z. Yang, H. Chen, Flash annealing yields a strong and ductile medium Mn steel with heterogeneous microstructure, Scr. Mater. 198 (2021) 113819.
[21] X. Wan, G. Liu, R. Ding, N. Nakada, Y.W. Chai, Z. Yang, C. Zhang, H. Chen, Stabilizing austenite via a core-shell structure in the medium Mn steels, Scr. Mater. 166 (2019) 68–72.
[22] X. Tan, W. Lu, X. Rao, Effect of ultra-fast heating on microstructure and mechanical properties of cold-rolled low-carbon low-alloy Q&P steels with different austenitizing temperature, Mater. Charact. 191 (2022) 112086.
[23] G. Liu, S. Zhang, J. Li, J. Wang, Q. Meng, Fast-heating for intercritical annealing of cold-rolled quenching and partitioning steel, Mater. Sci. Eng. A 669 (2016) 387–395.
[24] X. Gao, J. Liu, L. Bo, W. Chen, J. Sun, Z. Ning, A.H.W. Ngan, Y. Huang, Achieving superb mechanical properties in CoCrFeNi high-entropy alloy microfibers via electric current treatment, Acta Mater. 277 (2024) 120203.
[25] C. Lesch, P. Álvarez, W. Bleck, J. Gil Sevillano, Rapid transformation annealing: a novel method for grain refinement of cold-rolled low-carbon steels, Metall. Mater. Trans. A 38 (2007) 1882–1890.
[26] Y. Huang, F.J. Humphreys, Subgrain growth and low angle boundary mobility in aluminium crystals of orientation { 110} ⟨ 001 ⟩, Acta Mater. 48 (2000) 2017–2030.
[27] Y. Lü, D.A. Molodov, G. Gottstein, Recrystallization kinetics and microstructure evolution during annealing of a cold-rolled Fe-Mn-C alloy, Acta Mater. 59 (2011) 3229–3243.
[28] M.A. Mostafaei, M. Kazeminezhad, Bimodal grain size and mechanical properties enhancement in low carbon steel by ultra-rapid annealing, J. Mater. Res. Technol. 18 (2022) 2363–2367.
[29] M.A. Mostafaei, M. Kazeminezhad, Microstructure and mechanical properties improvement by ultra-rapid annealing of severely deformed low-carbon steel, Mater. Sci. Eng. A 655 (2016) 229–236.
[30] M.H. Mohammad-Ebrahimi, A. Zarei-Hanzaki, H.R. Abedi, S.M. Vakili, C. K. Soundararajan, The enhanced static recrystallization kinetics of a non-equiatomic high entropy alloy through the reverse transformation of strain induced martensite, J. Alloy. Compd. 806 (2019) 1550–1563.
[31] V. Sánchez-Alarcos, V. Recarte, D.L.R. Khanna, J. López-García, J.I. Pérez-Landazábal, Deformation induced martensite stabilization in Ni45Mn36.7In13.3Co5, Micro J. Alloy. Compd. 870 (2021) 159536.
[32] S. Kustov, J. Pons, E. Cesari, J. Van Humbeeck, Chemical and mechanical stabilization of martensite, Acta Mater. 52 (2004) 4547–4559.
[33] Z.H. Cai, H. Ding, R.D.K. Misra, Z.Y. Ying, Austenite stability and deformation behavior in a cold-rolled transformation-induced plasticity steel with medium manganese content, Acta Mater. 84 (2015) 229–236.
[34] I. Shakhova, V. Dudko, A. Belyakov, K. Tsuzaki, R. Kaibyshev, Effect of large strain cold rolling and subsequent annealing on microstructure and mechanical properties of an austenitic stainless steel, Mater. Sci. Eng. A 545 (2012) 176–186.
[35] X. Luo, T. Huang, Y. Wang, Y. Xin, G. Wu, Strong and ductile AZ31 Mg alloy with a layered bimodal structure, Sci. Rep. 9 (2019) 5428.
[36] J. Su, D. Raabe, Z. Li, Hierarchical microstructure design to tune the mechanical behavior of an interstitial TRIP-TWIP high-entropy alloy, Acta Mater. 163 (2019) 40–54.
[37] J. Ahmed, M. Daly, Yield strength insensitivity in a dual-phase high entropy alloy after prolonged high temperature annealing, Mater. Sci. Eng. A 820 (2021) 141586.
[38] Y. Yuan, J.J. Wang, J. Wei, W.Y. Chen, H.L. Yan, N. Jia, Cu alloying enables superior strength-ductility combination and high corrosion resistance of FeMnCoCr high entropy alloy, J. Alloy. Compd. 970 (2024) 172543.
[39] Z. Fu, P. Wu, S. Zhu, K. Gan, D. Yan, Z. Li, Effects of interstitial C and N on hydrogen embrittlement behavior of non-equiatomic metastable FeMnCoCr high-entropy alloys, Corros. Sci. 194 (2022) 109933.
[40] Y. Han, H. Li, H. Feng, K. Li, Y. Tian, Z. Jiang, Simultaneous enhancement in strength and ductility of Fe50Mn30Co10Cr10 high-entropy alloy via nitrogen alloying, J. Mater. Sci. Technol. 65 (2021) 210–215.
[41] E.D. Tabachnikova, T.V. Hryhorova, S.E. Shumilin, I.V. Kolodiy, Y.O. Shapovalov, Y.O. Semerenko, S.N. Smirnov, I.V. Kashuba, M.A. Tikhonovsky, M.J. Zehetbauer, E. Schafler, Mechanical properties of a two-phase high-entropy Fe50Mn30Co10Cr10 alloy down to ultralow temperatures, Low Temp. Phys. 48 (2022) 845–852.
[42] Z. Pan, T. Liu, J. Li, L. Wang, T. Zhang, J. Wang, Q. Tao, Improving mechanical properties of a forged high-Manganese alloy by regulating carbon content and carbide precipitation, Metals 12 (2022) 473.
[43] N. Meena, V. Srivastava, P. Srinivas, M. Gajendra, D.S. Gowtam, A.G. Rao, N. Prabhu, Elastic-plastic fracture toughness of wrought dual-phase non-equiatomic high-entropy alloy (HEA) for structural applications, Trans. Indian Inst. Met. 76 (2023) 1741–1750.
[44] E.O. Hall, The deformation and ageing of mild steel: III discussion of results, Proc. Phys. Soc. B 64 (1951) 747.
[45] P.H. Chang, A.G. Preban, The effect of ferrite grain size and martensite volume fraction on the tensile properties of dual phase steel, Acta Met. 33 (1985) 897–903.
[46] F. Trichter, A. Rabinkin, M. Ron, A. Sharfstein, A study of $\gamma \rightarrow \varepsilon$ phase transformation in Fe-Mn alloys induced by high pressure and plastic deformation, Scr. Met. 12 (1978) 431–434.
[47] M. Mazinani, W.J. Poole, Effect of martensite plasticity on the deformation behavior of a low-carbon dual-phase steel, Metall. Mater. Trans. A 38 (2007) 328–339.
[48] Q. Lai, L. Brassart, O. Bouaziz, M. Gouné, M. Verdier, G. Parry, A. Perlade, Y. Bréchet, T. Pardoen, Influence of martensite volume fraction and hardness on the plastic behavior of dual-phase steels: experiments and micromechanical modeling, Int. J. Plast. 80 (2016) 187–203.
[49] P. Sathiyamoorthi, H.S. Kim, High-entropy alloys with heterogeneous microstructure: Processing and mechanical properties, Prog. Mater. Sci. 123 (2022) 100709.